



Growth of g-C₃N₄ on mesoporous TiO₂ spheres with high photocatalytic activity under visible light irradiation

Xiaofang Chen^{a,b}, Jing Wei^a, Rujing Hou^c, Yan Liang^a, Zongli Xie^b, Yonggang Zhu^b,
Xiwang Zhang^a, Huanting Wang^{a,*}

^a Department of Chemical Engineering, Monash University, Clayton, VIC 3800, Australia

^b CSIRO Manufacturing, Private Bag 10, Clayton South, VIC 3169, Australia

^c The Education Ministry Key Lab of Resource Chemistry, Shanghai Normal University, 100 Guilin Road, Shanghai 200234, China

ARTICLE INFO

Article history:

Received 22 December 2015

Received in revised form 25 January 2016

Accepted 4 February 2016

Available online 6 February 2016

Keywords:

g-C₃N₄

Mesoporous TiO₂

TiO₂/g-C₃N₄

Heterostructure

Photocatalytic degradation

ABSTRACT

Growth of graphitic carbon nitride on mesoporous TiO₂ spheres with well-controlled structures was achieved by melt-infiltrating dicyandiamide (DICY). The molten DICY diffused into the porous structure of TiO₂, and g-C₃N₄ was produced inside the mesopores formed by packing of TiO₂ nanoparticles at higher temperature, resulting in a better fused g-C₃N₄-TiO₂ heterostructure. The formation of a strong interfacial connection between TiO₂ and g-C₃N₄ by this preparation method greatly improved the separation efficiency of photo-generated electrons and holes. TiO₂/g-C₃N₄ composites exhibited much higher photocatalytic activity than TiO₂ and g-C₃N₄ towards the degradation of Rhodamine B under both UV light and UV–vis light irradiation. The heterostructured combination provided a synergistic photocatalytic activity through an efficient electron transfer process. Based on the experimental results, a possible mechanism for the improved photocatalytic performance was proposed. The factors affecting the photocatalytic activity were also discussed based on the result of structure analysis, optical and photoelectric characteristics, and photocatalytic reactions.

© 2016 Elsevier B.V. All rights reserved.

1. Introduction

Harvesting solar light by semiconductors for production of green energy [1,2], wastewater treatment [3,4] and solar cell [5,6] is considered as a promising solution to address the imperative energy and environment issues. Titanium dioxide (TiO₂), as one of the most efficient semiconductors, has been vastly studied for many applications such as hydrogen evolution [7,8], CO₂ reduction [2,9] and wastewater treatment [4,10,11]. However, the large band gap of titanium dioxide (~3.2 and ~3.0 eV for anatase and rutile, respectively) limits its practical application, since it only effectively absorbs UV light that accounts for about 5% of solar light [10,12]. Recently, significant progress in the modification of TiO₂ for enhanced solar light absorption has been achieved by means of non-metal elements doping [13–15], metal deposition [16,17], and formation of heterostructures [18,19]. In the case of heterojunction semiconductors, a metal-free visible light photocatalyst, polymeric graphitic carbon nitride (g-C₃N₄), has been considered as one of the

ideal candidates to couple with TiO₂ [20,21]. This is because g-C₃N₄ satisfies the basic requirements for organic-pollutants degradation and water-splitting catalyst, owing to its high thermal and chemical stability and response to visible light [22,23–26]. Furthermore, the appealing electronic band structures of g-C₃N₄ could be tuned by further modification, which makes g-C₃N₄ a promising and versatile semiconductor for sunlight harvesting. However, the key issues with fast charge recombination and poor conductivity need to be addressed to improve g-C₃N₄ photocatalytic performance.

Research has shown that coupling g-C₃N₄ with other semiconductors with more positive conduction band can be a promising strategy for designing high-performance photocatalysts under visible light [3,27]. The combination of g-C₃N₄ with other semiconductors enables the photo-induced electrons to transfer to the band gap of coupled semiconductors and thus inhibits them from recombining with holes. In particular, coupling TiO₂ with g-C₃N₄ has been carried out to improve catalytic performance of individual TiO₂ and g-C₃N₄ on the basis of more negative conduction band of g-C₃N₄ than TiO₂. Many methods have been reported to synthesize TiO₂/g-C₃N₄ composite catalysts, e.g., N-TiO₂/g-C₃N₄ nanofibers synthesized via electrospinning and heat-etching process [28], TiO₂/C₃N₄ composites prepared by ball milling method [29], C and N co-doped TiO₂/g-C₃N₄ microspherical nanorods fabricated

* Corresponding author.

E-mail addresses: huanting.wang@monash.edu,
huanting.wang@eng.monash.edu.au (H. Wang).

by a thermal transformation method [18], and C_3N_4 -hybridized TiO_2 nanosheets obtained by solvent evaporation method [19]. Although forming a C_3N_4 - TiO_2 heterojunction structure has proved effective for improving photocatalytic activity, it is challenging to produce such a heterostructure with well interconnected TiO_2 and $g-C_3N_4$ phases. The barriers formed on the interface of heterojunction inevitably block the migration of charge carriers, leading to high rate of photo-generated electron-hole-pairs recombination. In addition, even though various synthesis methods have been explored, TiO_2 and $g-C_3N_4$ are not uniformly composited in terms of dispersion of TiO_2 nanoparticles in $g-C_3N_4$ nanolayers in many $TiO_2/g-C_3N_4$ composites reported in the literature. Also the wrapping of $g-C_3N_4$ on TiO_2 particles is difficult to control. These issues lead to poor interfacial connection, which thus blocks fast migration of the photo-generated carrier charges. Therefore, it is still a great challenge to realize synergistic functions in the heterostructure.

The main objective of this study is to develop a simple and effective method for synthesis of $TiO_2/g-C_3N_4$ composites with improved synergistic effects of heterostructured semiconductors. In particular, melting of a precursor of $g-C_3N_4$ into a mesoporous TiO_2 (M- TiO_2) enables growth of $g-C_3N_4$ with controllable coverage and thickness. As described in Scheme 1, the precursor of $g-C_3N_4$, DICY, can be melted at 190 °C and thus used to fill the mesopores of TiO_2 . Subsequently, during carbonization of DICY, $g-C_3N_4$ could be controlled to grow on M- TiO_2 spheres. Such a method provides a much better contact between the coupled semiconductors, facilitating the electron transfer. Our experiments show that the resulting $TiO_2/g-C_3N_4$ exhibits a high photocatalytic activity for photodegradation of organic pollutants and high stability for long and repeated usage.

2. Experimental

2.1. Preparation of photocatalysts

All reactants in this work were purchased from Sigma-Aldrich, Australia and used without further purification. M- TiO_2 was synthesized as follows. Hydrocellulose (DHC) (0.2 g) was firstly dissolved in the solution with absolute ethanol (95 mL) and deionized water (400 μ L), and then titanium (IV) butoxide (4.0 mL) was added dropwise in the above solution slowly. After vigorous stirring for 12 h, the sample was collected by centrifugation, followed by washing with absolute ethanol and deionized water, and drying in an oven at 70 °C for 4 h. Subsequently, it was transferred into an alumina crucible and calcined at 500 °C for 2 h at a heating rate of 2 °C min⁻¹ in a muffle furnace under air atmosphere. A given amount of dicyandiamide (DICY) was ground with the as-prepared M- TiO_2 (weight ratios of M- TiO_2 to DICY: 1:7.5, 1:5.0, and 1:3.0). Finally, the mixture was calcined in a tube furnace at argon atmosphere at different temperatures (190, 240, 400, 520 and 550 °C) for 2 h, and the heating rate was 10 °C min⁻¹. The final M- TiO_2 and $g-C_3N_4$ composites are denoted as x: y- $TiO_2/g-C_3N_4$ -z, where x: y means the weight ratio of M- TiO_2 and DICY and z is denoted calcination temperature. To further investigate the formation of $g-C_3N_4$ on M- TiO_2 , the mixture of M- TiO_2 and $g-C_3N_4$ was heated from ambient temperature to 190 °C, following a heating directly from 240 to 550 °C with a heating rate of 10 °C min⁻¹, and finally keeping the temperature at 550 °C for 2 h. This obtained sample was noted as $TiO_2/g-C_3N_4$ (0). In addition, the heating rate at the temperature range from 190 to 240 °C was adjusted to 0.5 °C min⁻¹ as well to keep the molten state of DICY for longer time and the prepared sample was noted as $TiO_2/g-C_3N_4$ (100). For comparison, $g-C_3N_4$ was also synthesized by directly calcining DICY under argon atmosphere at 550 °C for 2 h.

To evaluate the electron transfer between $g-C_3N_4$ and $TiO_2/g-C_3N_4$, another sample $TiO_2/g-C_3N_4$ (same stoichiometric ratio as the sample 1:5.0- $TiO_2/g-C_3N_4$) was prepared by mixing the as-prepared bulk $g-C_3N_4$ with stoichiometric M- TiO_2 using the grinding method.

2.2. Characterization

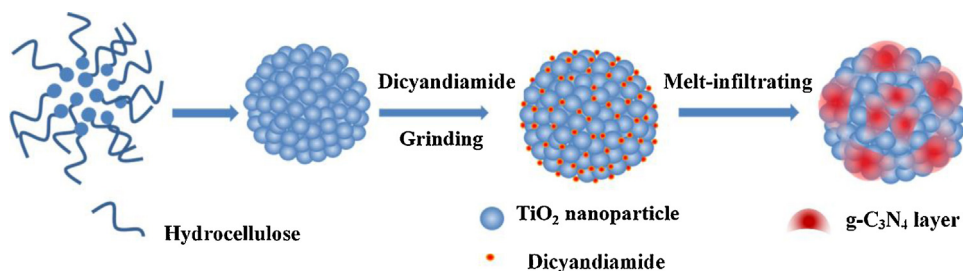
Powder X-ray diffraction (XRD) patterns of the samples were collected using a Miniflex 600 diffractometer (Rigaku, Japan) with Cu-K α radiation (15 Ma and 40 kV). The morphology of the samples was observed by field emission scanning electron microscopy (FESEM) utilizing a Nova NanoSEM 450 (FEI, USA) with an operating voltage of 3 kV. Transmission electron microscopy (TEM) images were taken by a FEI Tecnai G2 T20 and FEI Tecnai G2 F20 operated at an accelerating voltage of 200 kV. The thermogravimetry (TG) and differential thermal analysis (DTA) were conducted by a thermogravimetric analyzer (DTG-60H) under nitrogen atmosphere. The nitrogen adsorption-desorption isotherms of the samples was measured on a physisorption analyzer (Micromeritics ASAP 2020, USA) at liquid nitrogen temperature. Fourier transform infrared spectra (FT-IR) were recorded by a FTIR spectrophotometer (PerkinElmer Spectrum 100, USA) using the KBr wafer technique. Diffuse reflectance UV–vis absorption spectroscopy was performed with a UV-2600 (Shimadzu, USA) spectrophotometer with BaSO₄ as a reference. X-ray photoelectron spectroscopy (XPS, Versa Probe PHI 5000) was employed to determine surface electronic states. The shift of the binding energy due to the relative surface charging was corrected through using the C 1s peak at 284.8 eV as an internal standard. Photoluminescence (PL) spectra of samples was measured on a Varian Cary-Eclipse at room temperature (excitation wavelength = 325 nm).

2.3. Electrochemical measurements

Photoelectrochemical measurements were performed in a three-electrode, single-compartment quartz cell on an electrochemical station (CHI 660). Samples on ITO glass with an active area of ca. 4.0 cm² (30 mg of photocatalyst) were prepared as the working electrode. The platinum sheet and saturated calomel electrode (SCE) were served as the counter electrode and reference electrode, respectively. Besides, a bias voltage of 0.5 V was used for driving the photo-generated electrons transfer from the working electrode to the platinum electrode. The light source (300 W xenon lamp with ultraviolet filter ($\lambda > 400$ nm)) was mounted 10.0 cm away from the photoelectrochemical cell. A 0.20 M Na₂SO₄ aqueous solution worked as the electrolyte.

2.4. Photocatalytic activity

Rhodamine B (RhB) was used a probe dye to evaluate the photocatalytic activity of the as-prepared $TiO_2/g-C_3N_4$ composites under a 500 W xenon lamp (CHF-XM-500, at a light intensity of 100 mW cm⁻²) located at a distance of 10.0 cm. Typically, in a photo-degradation experiment, 50 mg of the as-prepared photocatalyst was dispersed with constant stirring in a 50 mL RhB aqueous solution (10 mg L⁻¹). Prior to illumination, the solution was kept in dark for 60 min and stirred to reach an adsorption-desorption equilibrium on the photocatalyst. At given intervals, the sample was taken and the suspension was centrifuged for 5 min to discard the sediment. The absorbance of the supernatant was measured by an UVmini-1240 UV–vis Spectrophotometer (Shimadzu, USA) at the characteristic wavelength of 553 nm. To analyze the photocatalytic activity of photocatalyst under visible light, an UV cut-off filter ($\lambda > 400$ nm) was used. The photodegradation of phenol was carried out as described above, where the concentration of



Scheme 1. Schematic illustration of the preparation of $\text{TiO}_2/\text{g-C}_3\text{N}_4$ microspheres.

phenol was 10 mg L^{-1} with a characteristic wavelength of 270 nm. To evaluate the stability of photocatalyst, after the photocatalytic reaction, the photocatalyst was collected by centrifugation, washing and drying for the recycling test.

3. Results and discussion

3.1. Formation of $\text{TiO}_2/\text{g-C}_3\text{N}_4$

To understand the formation of $\text{TiO}_2/\text{g-C}_3\text{N}_4$, the crystal structure and morphology of M- TiO_2 , $\text{g-C}_3\text{N}_4$ and $\text{TiO}_2/\text{g-C}_3\text{N}_4$ were firstly investigated. As shown in XRD patterns (Fig. 1a), $\text{g-C}_3\text{N}_4$ and anatase TiO_2 peaks can be clearly observed in the sample of $\text{TiO}_2/\text{g-C}_3\text{N}_4$. Specifically, peaks at 25.3, 36.9, 37.8, 38.6, 48.0, 53.9, 55.1, 62.6, 68.8, 70.1, and 75.0° are attributed to (101), (103), (004), (112), (200), (105), (211), (204), (116), (220), and (215) planes, respectively, which arise from the tetragonal phase of anatase TiO_2 crystals (JCPDF No. 21-1272) [19,30]. The peak at 13.1° is indexed to the (100) plane of tri-s-triazine units and the peak at 27.4° is attributed to the (002) reflection, the latter corresponding to the interlayer stacking of the aromatic segments with an interlayer distance of $d = 0.321 \text{ nm}$ in a good agreement with the literature [31,32]. In addition, the peaks assigned to $\text{g-C}_3\text{N}_4$ can be easily observed in the sample of $\text{TiO}_2/\text{g-C}_3\text{N}_4$.

The morphology and microstructure shown in the FESEM images in Fig. 1 provide further evidence of growth of $\text{g-C}_3\text{N}_4$ layer on the M- TiO_2 spheres. The high-magnification FESEM image (Fig. 1b) reveals that the white sample obtained by the sol-gel method and DHC surfactant modification shows well-defined microsphere morphology. Obviously, these microspheres with diameters around 300–500 nm are formed by the packing of small TiO_2 nanoparticles. The N_2 adsorption/desorption isotherms in Fig. S1 confirms the presence of mesoporous structure. On the basis of the adsorption branch (Fig. S1, inset), the pore size is calculated to be approximately 10 nm, formed by the packing of small nanoparticles. This structure is essential for $\text{g-C}_3\text{N}_4$ growth inside M- TiO_2 . However, after the formation of $\text{g-C}_3\text{N}_4$, the 10 nm pore structure disappears, indicating that these M- TiO_2 pores are filled with the molten DICY and thus $\text{g-C}_3\text{N}_4$ possibly is formed inside the pores. When M- TiO_2 is coupled with $\text{g-C}_3\text{N}_4$, the colour of 1:5.0- $\text{TiO}_2/\text{g-C}_3\text{N}_4$ sample turns yellowish green as shown in Fig. 1c (inset). Also, it can be seen that the hybridized $\text{g-C}_3\text{N}_4$ layer partially covers the surface of M- TiO_2 mesoporous spheres in Fig. 1c. In a higher-magnification FESEM image (Fig. 1d), it appears that TiO_2 particles are not fully covered by $\text{g-C}_3\text{N}_4$, and they are partially exposed. The simulated structure is shown in the inset of Fig. 1d. The partially covering of TiO_2 can be considered as strong evidence for the proposed formation process of $\text{TiO}_2/\text{g-C}_3\text{N}_4$. More importantly, when this photocatalyst works under sunlight irradiation, the partially exposed TiO_2 is beneficial to photo-generated holes to contact with H_2O , dissolved O_2 , and pollutants, which can promote the production of active radicals in photocatalytic reaction system.

To investigate the growth mechanisms of $\text{g-C}_3\text{N}_4$, the condensation steps of DICY were studied by TG-DTA. Fig. S2 clearly exhibits the endothermic melting of DICY at 214°C without any weight loss. Subsequently, the exothermic reaction to melamine is at about 245°C and thus the weight presents a slightly loss. The following weight loss at around 350°C is caused by the partial sublimation [33]. Finally, the condensation step takes place at approximately 410°C. In order to study the contribution of molten state of DICY, TEM and X-ray were used to monitor the morphology and crystal structure changes of samples prepared by keeping the molten state of DICY for a certain period of time at the temperature range from 190 to 240°C. For $\text{TiO}_2/\text{g-C}_3\text{N}_4$ (0), little $\text{g-C}_3\text{N}_4$ can be observed on M- TiO_2 at the beginning as shown in Fig. 2a. Even in HRTEM image (Fig. 2d), no $\text{g-C}_3\text{N}_4$ layer can be observed, except for the lattice fringes for the identification of crystallographic spacing of ca 0.35 nm. However, for $\text{TiO}_2/\text{g-C}_3\text{N}_4$, $\text{g-C}_3\text{N}_4$ nanolayer can be evidently observed when extending the time to 5 min by controlling the heating rate for $10^\circ\text{C min}^{-1}$ at that temperature range (Fig. 2b). By magnifying this image, it can be clearly measured that the thickness of $\text{g-C}_3\text{N}_4$ layer is around 10 nm, but it is not very uniform. In HRTEM image of $\text{TiO}_2/\text{g-C}_3\text{N}_4$ (Fig. S3), the interface between TiO_2 and $\text{g-C}_3\text{N}_4$ and lattice fringes of TiO_2 can be clearly observed. Subsequently, extending the heating time to 100 min by decreasing the heating rate to $0.5^\circ\text{C min}^{-1}$, the $\text{g-C}_3\text{N}_4$ layer can be detected easily (Fig. 2c). Its thickness increases to average around 25 nm and tends to be uniform. The nitrogen and carbon atoms were distributed on mesoporous TiO_2 sphere shown in Fig. S4, determined via scanning transmission electron microscopy (STEM) and element mapping technique.

In the case of crystal structure, the main peaks of DICY can be still observed in Fig. 3 in the sample of 1.50- $\text{TiO}_2/\text{g-C}_3\text{N}_4$ -190. Further increasing the heating treatment temperature to 240°C, partial DICY started converting to melamine, possibly as a result of the exothermic reaction from DICY to melamine at 245°C [33]. This result is consistent with FI-IR analysis in Fig. S5. Compared 1.50- $\text{TiO}_2/\text{g-C}_3\text{N}_4$ -190 with DICY, the peak at around 2200 cm^{-1} assigned to the C=N stretching frequency of DICY is extremely weak and the peaks located at 1502 and 1636 cm^{-1} assigned to the characteristic peaks of DICY are broaden. Further increasing the temperature to 240°C, the peaks at 1406–1642 matching the characteristic infrared peaks of melamine become stronger, which means that DICY experienced the molten state and then converted into melamine [38]. Based on the above results, it can be evidently revealed that by controlling the time at the temperature range (190–240°C), DICY could be kept as the molten state and gradually polymerize into bigger molecule. The molten state allows DICY to fill into the pores of M- TiO_2 . The analysis demonstrates that the porous structure of M- TiO_2 and the molten state of DICY contribute to the formation of $\text{g-C}_3\text{N}_4$ growing on M- TiO_2 .

In addition to the study on molten state of DICY, the M- TiO_2 /DICY ratio and the heating temperature for polymerizing of DICY were also investigated. In Fig. S6, in the $\text{TiO}_2/\text{g-C}_3\text{N}_4$ composite, the M- TiO_2 microsphere is composed of small TiO_2 crystallites

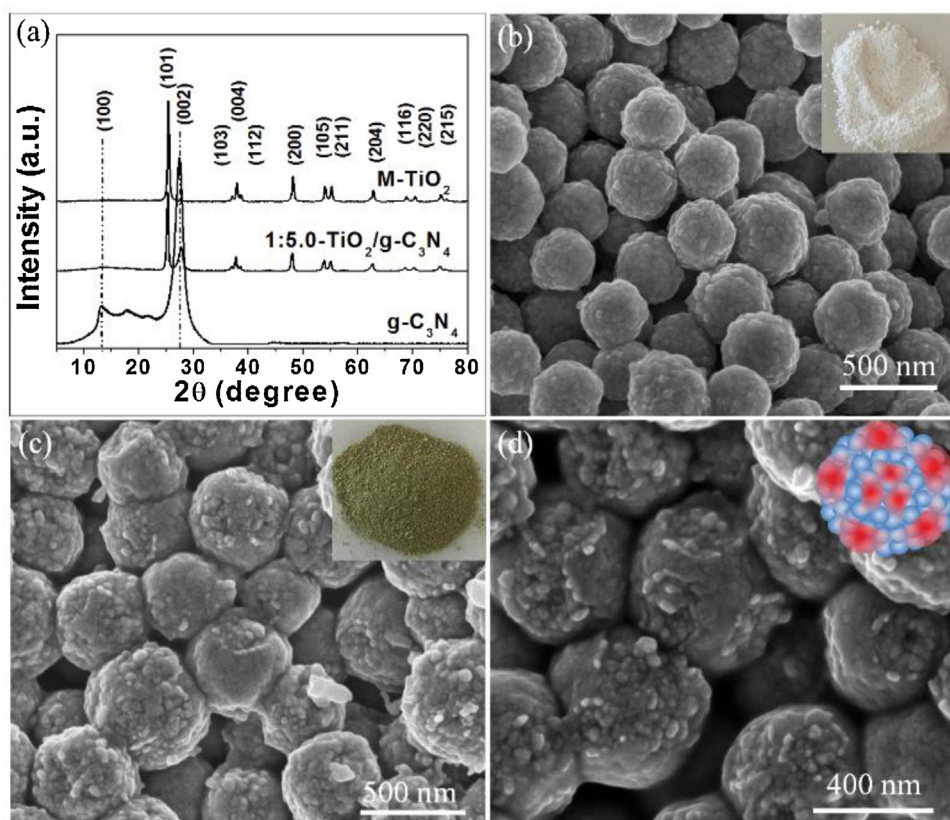


Fig. 1. (a) XRD patterns of M-TiO₂, 1:5.0-TiO₂/g-C₃N₄, and g-C₃N₄ samples; (b–d) FESEM images of (b) M-TiO₂ (inset: digital photo of M-TiO₂), (c) and (d) 1:5.0-TiO₂/g-C₃N₄, (inset in (c): digital photo of 1:5.0-TiO₂/g-C₃N₄). (For interpretation of the references to color in the text, the reader is referred to the web version of this article.)

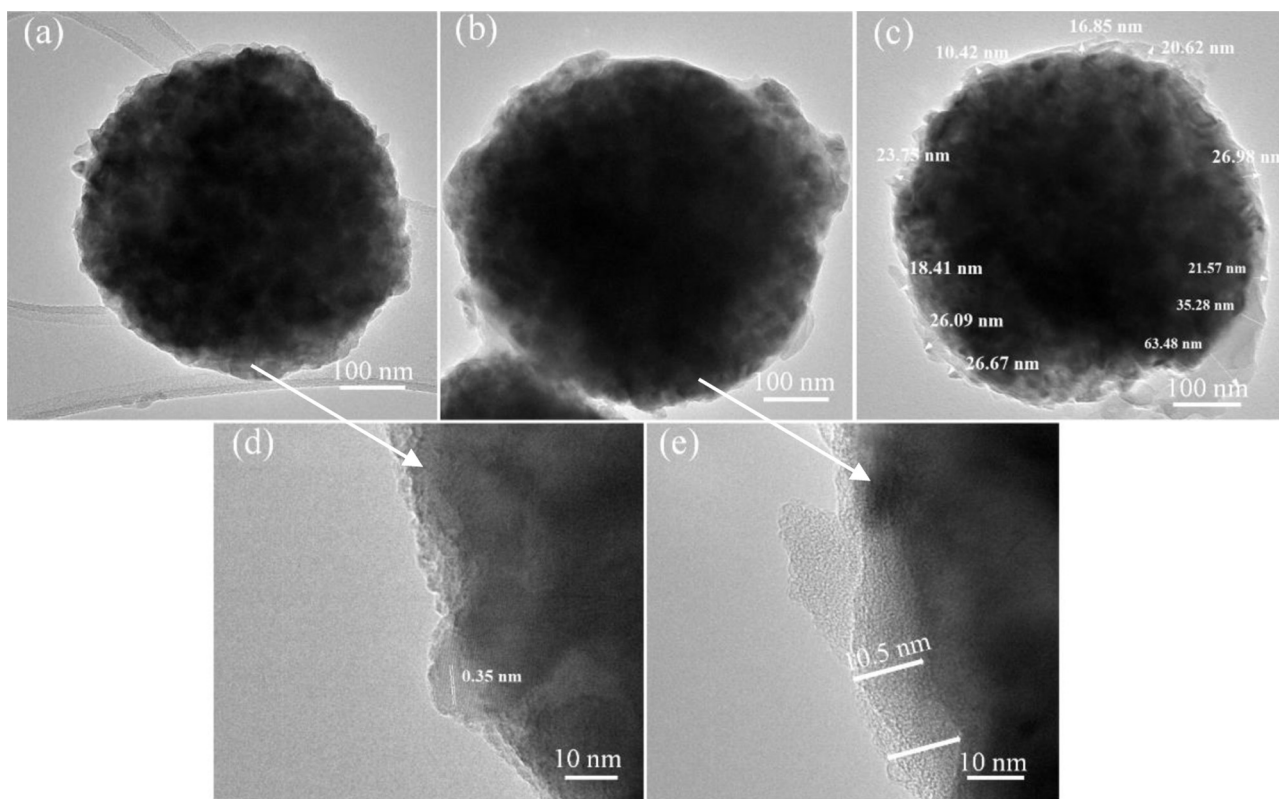


Fig. 2. TEM images showing the effects of the molten DIC on growth of g-C₃N₄ layer on M-TiO₂, (a) TiO₂/g-C₃N₄ (0) obtained by heating the sample from room temperature to 190 °C and subsequent heating again directly from 240 to 550 °C with a heating rate of 10 °C min⁻¹, (b) 1:5.0-TiO₂/g-C₃N₄ with a heating rate of 10 °C min⁻¹ at the temperature range from 190 to 240 °C, (c) TiO₂/g-C₃N₄ (100) synthesized by decreasing the heating rate to 0.5 °C min⁻¹ at the range of temperature from (190–240 °C), and (d) and (e) HRTEM of (a) and (b), respectively.

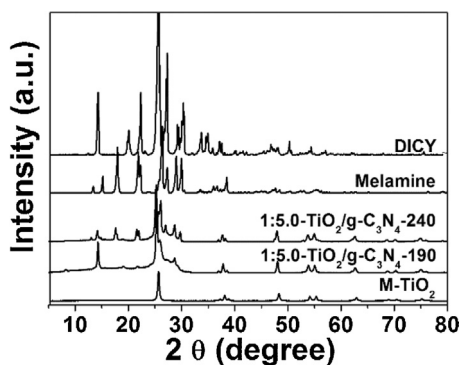


Fig. 3. XRD diffraction pattern to trace the formation of g-C₃N₄ on M-TiO₂ surface. XRD patterns of samples: DICY, Melamine, 1:5.0-TiO₂/g-C₃N₄-240, 1:5.0-TiO₂/g-C₃N₄-190 and M-TiO₂.

with a size of about 24 nm, calculated using the Scherrer equation, i.e.,

$$D = K\lambda / B \cos \theta,$$

where B is the half-height width of the diffraction peak of anatase, $K=0.89$ is a coefficient, θ is the diffraction angle, and λ is the X-ray wavelength corresponding to the Cu K α irradiation [4,22]. Increasing the amount of DICY, the particle size becomes smaller, as described in Table S1, especially compared to pure TiO₂. This change is possibly explained by nitrogen doping, since the dopants could restrain the growth of crystals [30]. Moreover, the annealing temperature affects the crystallinity of g-C₃N₄ on M-TiO₂ mesoporous spheres, as indicated in Fig. S7. For example, when increasing annealing temperature from 400 to 550 °C, the characteristic peak at 27.4 becomes sharper, and slightly shifts to higher angle with inter planar distance of aromatic unit dropping by 0.037 Å, indicating much denser structure obtained because of the localization of the electrons and stronger binding between layers [23,33].

To further demonstrate the existence of g-C₃N₄ in the as-obtained sample of 1:5.0-TiO₂/g-C₃N₄, IR and XPS were used to analyze the molecular structure and chemical state of elements (C, N and Ti) in Fig. S8. Pure g-C₃N₄ and 1:5.0-TiO₂/g-C₃N₄ were studied by FT-IR spectroscopy (Fig. S8a). Several strong bands are observed for two samples in the region from 1200 to 1700 cm⁻¹, which can be ascribed to the typical stretching modes of CN heterocycles with peaks at 1630, 1575, 1319, and 1228 cm⁻¹, respectively [18,31]. The peak at around 805 cm⁻¹ is attributed to the characteristic breathing mode of tri-s-triazine units. These results further indicate the existence of the g-C₃N₄ in TiO₂/g-C₃N₄ composites. The surface chemistry of M-TiO₂ and TiO₂/g-C₃N₄ was analyzed by XPS analysis. The chemical status of the Ti, C, and N elements was identified in the as-prepared samples. A curve fitting analysis of N 1s XPS spectra (Fig. S8b) reveals that two peaks at 398.7 and 400.2 eV can be ascribed to the sp²-hybridized nitrogen (C=N-C) and tertiary nitrogen (N-C₃), respectively. Moreover, as shown in the high-resolution Ti 2p spectrum (Fig. S8c), peaks at 458.8 and 464.5 are assigned to Ti 2p_{3/2}, and Ti 2p_{1/2} of TiO₂ [34]. Compared with M-TiO₂, the peaks do not show any shift to higher or lower binding energy [35]. Furthermore, no obvious peaks of Ti-N can be observed in Fig. S8d, presumably due to a low content of doped nitrogen in this sample. It can be easily seen that there are two peaks located at 284.8 and 288.3 eV. The former is ascribed to the binding energy of the sp² hybridized carbon, while the latter is due to N-C=N coordination [35]. Therefore, based on the results of XRD diffraction, FT-IR, and XPS, TiO₂/g-C₃N₄ is composed of g-C₃N₄ and M-TiO₂ possibly doped with a small content of nitrogen.

3.2. Optical characteristics

In order to investigate the optical properties of TiO₂/g-C₃N₄ materials, UV-vis diffuse reflectance spectroscopy (DRS) was carried out. The UV-vis absorption spectrum (Fig. 4a) shows remarkable redshift for the TiO₂/g-C₃N₄ composites in comparison with M-TiO₂. This implies that more visible light can be harvested by TiO₂/g-C₃N₄. By plotting $(\alpha h\nu)^{1/2}$ vs photon energy, the band gap energy can be determined (Fig. 4b). Band gaps of M-TiO₂, 1:5.0-TiO₂/g-C₃N₄, and g-C₃N₄ are 3.09, 2.53, and 2.62 eV, respectively. Obviously, the hybrid structure contributes to the widened light absorption region. For TiO₂/g-C₃N₄ composites, the improved harvest of light could be attributed to nitrogen dopant in the composite produced in the heat-etching process.

In general, the photocatalytic activity positively relates to light harvesting, charge separation and charge injection for heterostructured semiconductors. The lifetime of photo-generated electron is less than decades of femtoseconds, so it is easy for photo-generated electron to recombine together with photo-generated hole [36]. Therefore, apart from the visible light harvesting, free diffusion path for photo-generated carrier charge transfer is important to the improvement of the photocatalytic activity. The heterostructured combination of g-C₃N₄ and M-TiO₂ provides a much freer path for charge transfer because a strong interfacial connection between coupled semiconductors is the key to promote charge separations among heterostructures. In order to further demonstrate the TiO₂/g-C₃N₄ exhibits good interfacial connectivity, PL and photoelectrochemical analysis were performed. In Fig. 5a, g-C₃N₄ and M-TiO₂ have different emission peaks at 440 nm and 480 nm, which is consistent with those reported in the literature [35]. Compared with M-TiO₂ and Grinding-TiO₂/g-C₃N₄, g-C₃N₄ has the strongest peak, implying that it has the highest recombination rate of photo-induced electron/hole pairs. That can be explained by the narrow band gap of g-C₃N₄. In contrast, when 1:5.0-TiO₂/g-C₃N₄ is compared with Grinding-TiO₂/g-C₃N₄, no obvious peak at 460 nm of the 1:5.0-TiO₂/g-C₃N₄ sample is observed, which suggests photo-generated holes and electrons can be fast separated. According to the PL results, it can be demonstrated that the gap between TiO₂ and g-C₃N₄ obtained by physically mixing (Grinding-TiO₂/g-C₃N₄) inhibits the photo-generated electrons from transferring between conduction bands of coupled semiconductors. Photocurrent was measured for 1:5.0-TiO₂/g-C₃N₄, Grinding-TiO₂/g-C₃N₄, and g-C₃N₄ to study the photo-generated charge transfer efficiency. Fig. 5b illustrates a fast and steady photocurrent response for each light-on and light-off in both electrodes. It can be seen that the intensity of photocurrent is in the order of 1:5.0-TiO₂/g-C₃N₄ > Grinding-TiO₂/g-C₃N₄ > g-C₃N₄. Among them, the photocurrent response of 1:5.0-TiO₂/g-C₃N₄ reaches almost 3 times higher than that of Grinding-TiO₂, indicating that photo-generated electrons and holes can be separated and faster transferred as a result of the synergetic effect between TiO₂ and g-C₃N₄. In addition, the immediate drop of photocurrent after light removal implies a very short lifetime of photo-generated charges in samples g-C₃N₄ and Grinding-TiO₂/g-C₃N₄. Whereas the decay curve for 1:5.0-TiO₂/g-C₃N₄ exhibits a long tail. Such a long-lasting "dark current" clearly illustrates that a substantial separation of electrons and holes may be built within TiO₂/g-C₃N₄ heterostructure, which means this structure contributes to the long lifetime of photo-generated charges. Therefore the great enhancement of the photocurrent in TiO₂/g-C₃N₄ structure should be promoted by enhanced light harvest and highly improved charge transfer efficiencies induced by good interfacial connection. As shown in Fig. 5c, the EIS reveals that the process of charge transfer more deeply. The arc radius reflects the charge-transfer resistance. Obviously, all samples exhibit a slight drop of resistance under light illumination than dark conditions, caused by the fill-

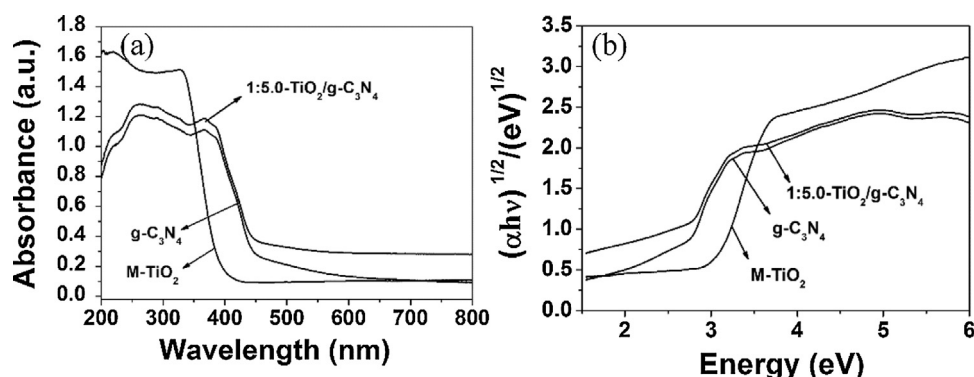


Fig. 4. (a) UV-vis absorption spectra of bulk $\text{g-C}_3\text{N}_4$, 1:5.0- $\text{TiO}_2/\text{g-C}_3\text{N}_4$ and M- TiO_2 , (b) plots of $(\alpha h\nu)^{1/2}$ vs photon energy of 1:5.0- $\text{TiO}_2/\text{g-C}_3\text{N}_4$, bulk $\text{g-C}_3\text{N}_4$, and M- TiO_2 ; $(\alpha h\nu)^{1/2}$ is determined from the UV-vis diffuse reflectance spectra, according to the equation: $(\alpha h\nu)^n = A(h\nu - E_g)$, where α , ν , A , and E_g are the absorption coefficient, light frequency, proportionality constant and bandgap, respectively. The value of n is determined by the property of materials. For $\text{g-C}_3\text{N}_4$, the n is $\frac{1}{2}$ for the indirect band gap semiconductor [30].

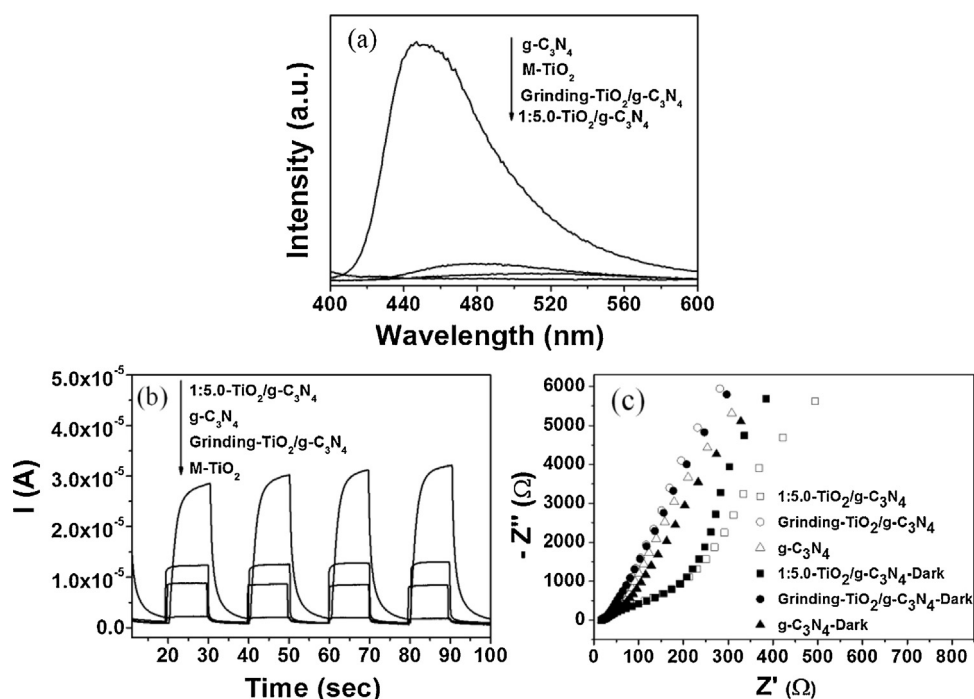


Fig. 5. (a) Photoluminescence spectra of the photocatalysts, (b) photocurrent versus time response of photoelectrode (0.5 V vs. SCE) under irradiation of visible light with wavelength >400 nm with 20 s light on/off cycles, and (c) Nyquist plot of electrochemical impedance spectra under visible irradiation.

ing of conduction band and value band with electrons and holes when illuminated. Furthermore, 1:5.0- $\text{TiO}_2/\text{g-C}_3\text{N}_4$ shows lower resistance in electron migration than Grinding- $\text{TiO}_2/\text{g-C}_3\text{N}_4$. These results indicate the well-controlled heterostructure of $\text{TiO}_2/\text{g-C}_3\text{N}_4$ provides a much more freedom for the migration of photo-generated charge carriers from bulk to the surface and between two connected semiconductors.

3.3. Photocatalytic performance

To further evaluate the migration efficiency of photo-induced charge carriers in well-connected heterostructures, the photocatalytic activity for RhB degradation by photocatalysts with different structures was investigated. As shown in Fig. 6a, in comparison with other photocatalysts, sample 1:5.0- $\text{TiO}_2/\text{g-C}_3\text{N}_4$ exhibits remarkably higher photocatalytic activity under visible light irradiation, and performs much better than the commercial TiO_2 (Degussa, P25). Obviously, the photocatalytic degradation of RhB

in the absence of photocatalysts is negligible. The M- TiO_2 shows very weak photocatalytic activity, because it merely absorbs UV light. On the other hand, $\text{g-C}_3\text{N}_4$ shows higher catalytic activity than M- TiO_2 , owing to powerful harvesting of visible light. For the Grinding- $\text{TiO}_2/\text{g-C}_3\text{N}_4$ sample, its photocatalytic activity is lower than 1:5.0- $\text{TiO}_2/\text{g-C}_3\text{N}_4$, although they share the same stoichiometry of M- TiO_2 and $\text{g-C}_3\text{N}_4$. This can be explained by their different microstructures. For Grinding- $\text{TiO}_2/\text{g-C}_3\text{N}_4$, simply mechanical mixing, without a chemical combination, generates a great gap between TiO_2 and $\text{g-C}_3\text{N}_4$, so that the photo-excited electrons in the conduction band are retarded to migrate to that of M- TiO_2 , leading to high recombination of electrons and holes finally. On the contrary, $\text{TiO}_2/\text{g-C}_3\text{N}_4$ heterojunction achieved by the melt-infiltration and growth method provides a better connectivity on the interface of $\text{g-C}_3\text{N}_4$ and M- TiO_2 . The interface between two coupled semiconductors promotes the direct migration of photo-generated charges from the band gap of $\text{g-C}_3\text{N}_4$ to that of M- TiO_2 . Moreover, a better heterostructured combination is also

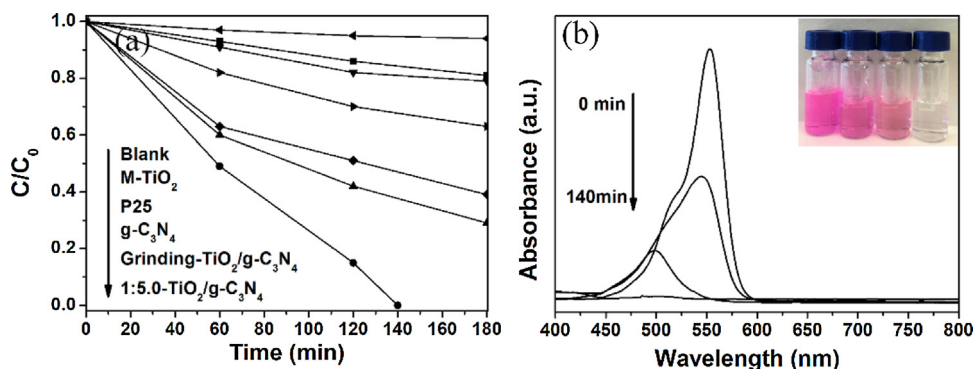


Fig. 6. (a) Photodegradation of RhB by M-TiO₂, bulk g-C₃N₄, P25, Grinding-TiO₂/g-C₃N₄, and 1:5.0-TiO₂/g-C₃N₄ under visible light irradiation ($\lambda > 400$ nm); for comparison, a control experiment was also conducted (i.e., blank, absence of photocatalyst). (b) Time-dependent UV-vis absorption spectra of the RhB solution in the presence of 1:5.0-TiO₂/g-C₃N₄ composite; the inset shows the colour-fading process of RhB solution with time when 1:5.0-TiO₂/g-C₃N₄ is used as the photocatalyst. Reaction conditions: 50 mg of catalyst, 50 mL of 10.0 mg L⁻¹ RhB aqueous solution, reaction time 3 h, reaction temperature 30 °C, one 500 W xenon lamp (light intensity 100 mW cm⁻², $\lambda > 400$ nm).

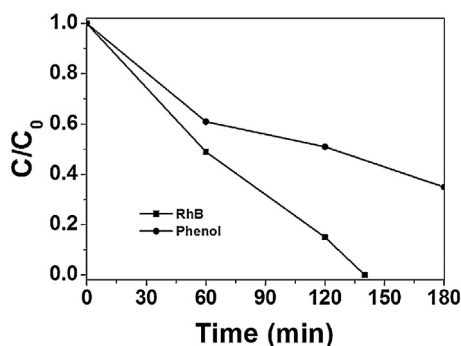


Fig. 7. The photocatalytic degradation of RhB and phenol, 1:5.0-TiO₂/g-C₃N₄ as the photocatalyst. Reaction conditions: 50 mg of catalyst, 50 mL of 10.0 mg L⁻¹ RhB or phenol aqueous solution, reaction time 3 h, reaction temperature 30 °C, one 500 W xenon lamp (light intensity 100 mW cm⁻², $\lambda > 400$ nm).

beneficial to improve the synergistic photocatalytic activity through an more efficient electrons transfer process. The favorable interfacial structure in 1:5.0-TiO₂/g-C₃N₄ composite is further evidence by the red shift of visible-light absorbance observed. The results show that the TiO₂/g-C₃N₄ heterojunction structure is much better than either pure M-TiO₂, bulk g-C₃N₄, or a mixture of g-C₃N₄ and coupled semiconductors. In Fig. 6b, although, the peak at 553 nm shows a gentle blue-shift, it disappears completely after 140 min, corresponding to the change of RhB solution colour in the inset.

Phenol was also used as a model organic compound for non-dye pollutants for degradation. It can be seen in Fig. 7 that RhB is more easily to be degraded than phenol under the same conditions; this is possibly due to the difference in their chemical stability as the benzene ring in phenol structure is more difficult to be decomposed [35]. However, even though phenol is difficult to be decomposed, almost 70% of phenol was degraded under visible light irradiation, which also further demonstrates that TiO₂/g-C₃N₄ has high photocatalytic activity in the degradation of organic pollutants. Significantly, the result also indicates that the high activity of TiO₂/g-C₃N₄ towards RhB degradation can be mainly attributed to photodegradation but not photosensitization process.

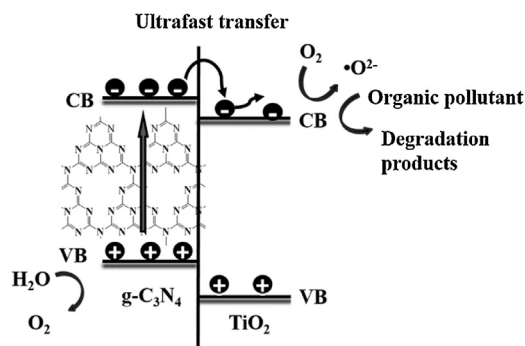
Additionally, M-TiO₂/DICY ratio also has some effects on the improvement of photocatalytic activity. Fig. S9 shows photodegradation of RhB under simulated solar light and visible light ($\lambda > 400$ nm) utilizing the photocatalysts prepared with different M-TiO₂/DICY ratios. As observed in Fig. S9a, under simulated sunlight irradiation, 1:7.5-TiO₂/g-C₃N₄ shows similar photocatalytic activity to M-TiO₂. When the ratio of M-TiO₂ to DICY decreases to 1:5.0, the photocatalytic activity of the photocatalyst significantly increases. In particular, RhB is decolorized completely within 40 min

when using 1:5.0-TiO₂/g-C₃N₄ photocatalyst, which is much faster than that of g-C₃N₄. However, with further reducing the M-TiO₂/DICY ratio to 1:3.0, the photocatalytic activity drops again, although it is still higher than g-C₃N₄. In the case of visible light irradiation, the variation of degradation efficiency of RhB utilizing the photocatalysts prepared with various M-TiO₂ and DICY ratios is similar to that under simulated sun light irradiation. As described in Fig. S9b, 1:5.0-TiO₂/g-C₃N₄ still exhibits the highest activity among all photocatalysts, in which 140 min was required for RhB complete degradation. On the contrary, almost no degradation occurs in the presence of M-TiO₂ due to its wide band gap. However the degradation rate of TiO₂/g-C₃N₄ under simulated sunlight irradiation is much higher than that under visible light irradiation. It might be caused by TiO₂ that can be excited by the light with short wavelength in the simulated sunlight. Potentially, the synergistic effect of TiO₂/g-C₃N₄ could also accelerate the degradation of RhB under simulated sunlight irradiation. The high photocatalytic activity and degradation rate imply that TiO₂/g-C₃N₄ heterostructure obtained by melt-infiltration method has the great potential for environmental remediation in industry. Furthermore, these results demonstrate that the ratio of TiO₂/g-C₃N₄ is an important factor affecting the photocatalytic activity of TiO₂/g-C₃N₄ photocatalyst, especially in the case of visible light irradiation.

The heating temperature is also an important factor to improve photocatalytic activity. As observed in Fig. S10, the photocatalyst obtained at 400 °C displays the lowest activity for degradation of RhB under visible light irradiation, while the photocatalytic activity of 1:5-TiO₂/g-C₃N₄ prepared at 550 °C is the highest. It can be attributed to the denser structure and enhanced polymerization of g-C₃N₄ heated at higher temperature, as indicated in Fig. S7 [23,25] and enhanced absorption towards visible light in Fig. S11. Moreover, higher temperature leads to better fusion of g-C₃N₄ into M-TiO₂, which greatly promotes migration of electrons from the conduction of g-C₃N₄ to that of M-TiO₂. However, the temperature cannot be further increased over 600 °C, because of decomposition of g-C₃N₄ under high temperature as reported [25].

3.4. Mechanism of enhancement photocatalytic activity

The high photocatalytic activity can be due to enhanced light harvesting and ultrafast transfer of photo-generated electrons at the heterostructured interface. Under visible light irradiation, the matched energy levels between TiO₂ and g-C₃N₄ firstly drive photo-generated electrons to transfer from the band gap (CB) of g-C₃N₄ to that of TiO₂, as illustrated in Scheme 2. Besides, the good connected interface provides a free path for charge transfer. Because fast charge transfer likely contributes to an accumula-



Scheme 2. Mechanism of fast charge transfer at the interface between g-C₃N₄ and TiO₂.

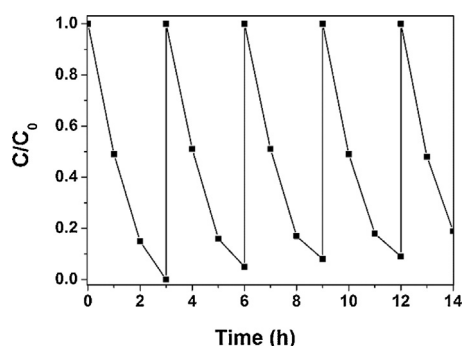


Fig. 8. Recycling tests of 1:5.0-TiO₂/g-C₃N₄ photocatalyst. Reaction conditions: 50 mg of catalyst, 50 mL of 10.0 mg L⁻¹ RhB aqueous solution, reaction time 3 h, reaction temperature 30 °C, light intensity 100 mW cm⁻², λ > 400 nm (one 500 W xenon lamp).

tion of electrons on the CB of TiO₂ and thus the accumulation of electrons are likely to change the internal field, which could drive the charge transfer. Furthermore, the structure of g-C₃N₄ is a layered network consisting of the tri-s-triazine structure, and it has a certain degree of disorder and delocalization of electrons after thermal condensation [7,37]. Therefore, at the interfaces of TiO₂ and g-C₃N₄, electronic delocalization is possible to exist at local crystallinity and extensive π -conjugation [7]. According to a recent report, electronic delocalization can lead to the highly efficient charge separation [37]. TiO₂ thus serves as an electron trap to promote the efficient separation of photo-generated electrons and holes. Finally, the acceptors (O₂ in solution) of electrons scavenge the electrons on the CB of semiconductors for the subsequent reduction reaction. Meanwhile, the photo-generated holes left on the valence band (VB) can oxidize the organic pollutants in the solution by direct and indirect oxidation. Additionally, the possible existence of nitrogen dopant in TiO₂ likely contributes to the more light-harvesting than pure TiO₂, so that both g-C₃N₄ and nitrogen-doped TiO₂ can be excited by visible light for the degradation of organic pollutants. In short, heterostructured combination provides a synergistic photocatalytic activity through an efficient electron transfer process.

3.5. Recyclability of TiO₂/g-C₃N₄ photocatalyst

To evaluate the lifetime of 1:5.0-TiO₂/g-C₃N₄, cycling experiments were carried out on RhB degradation under visible light irradiation for five times. As shown in Fig. 8, no significant decrease of activity was observed after being used repetitively for 5 times. The slight decrease of activity is possibly due to the deactivation of photocatalyst by the adsorbed impurities. This result indicates that TiO₂/g-C₃N₄ has high stability under light irradiation. Such

characteristics lay the foundation for industrial application of this photocatalyst.

4. Conclusion

TiO₂/g-C₃N₄ composite with well-controlled structure was synthesized by melt-infiltration of DICY and subsequent formation of g-C₃N₄. The melt-infiltration of DICY results in better fusion of g-C₃N₄ into M-TiO₂ and thus a strong interfacial connection between TiO₂ and g-C₃N₄, which are important in promoting both visible light adsorption and photo-generated electron transfer. The TiO₂/g-C₃N₄ catalyst presents highly photocatalytic activity used for degradation of organic pollutants because of the synergistic effect between M-TiO₂ and g-C₃N₄ nanosheets and possible N doping in TiO₂. This work provides a simple and effective method to reduce the barriers in composites to promote utilization efficiency of solar energy.

Acknowledgements

The authors thank the staff of Monash Centre for Electron Microscopy for their technical assistance in SEM and TEM, and acknowledge the technical support from Mr Glenn Bradbury of CSIRO Microfluidics Team. X.C. thanks Monash University and CSIRO for a New Horizons Scholarship.

Appendix A. Supplementary data

Supplementary data associated with this article can be found, in the online version, at <http://dx.doi.org/10.1016/j.apcatb.2016.02.012>.

References

- [1] H. Yan, H. Yang, J. Alloys Compd. 509 (2011) 26–29.
- [2] M.S. Hamdy, R. Amrollahi, I. Sinev, B. Mei, G. Mul, J. Am. Chem. Soc. 136 (2014) 594–597.
- [3] J. Yu, S. Wang, J. Low, W. Xiao, Phys. Chem. Chem. Phys. 15 (2013) 16883–16890.
- [4] Y. Huo, R. Hou, X. Chen, H. Yin, Y. Gao, H. Li, J. Mater. Chem. A 3 (2015) 14801–14808.
- [5] K.S. Leschkes, R. Divakar, J. Basu, E. Enache-Pommer, J.E. Boercker, C.B. Carter, U.R. Kortshagen, D.J. Norris, E.S. Aydil, Nano Lett. 7 (2007) 1793–1798.
- [6] B. Liu, E.S. Aydil, J. Am. Chem. Soc. 131 (2009) 3985–3990.
- [7] Y. Shiraishi, S. Kanazawa, Y. Sugano, D. Tsukamoto, H. Sakamoto, S. Ichikawa, T. Hirai, ACS Catal. 4 (2014) 774–780.
- [8] Y. Shiraishi, Y. Togawa, D. Tsukamoto, S. Tanaka, T. Hirai, ACS Catal. 2 (2012) 2475–2481.
- [9] Q. Liu, Z.X. Low, L. Li, A. Razmjou, K. Wang, J. Yao, H. Wang, J. Mater. Chem. A 1 (2013) 11563–11569.
- [10] Y. Huo, X. Chen, J. Zhang, G. Pan, J. Jia, H. Li, Appl. Catal. B 148–149 (2014) 550–556.
- [11] M. Xing, J. Zhang, F. Chen, Appl. Catal. B 89 (2009) 563–569.
- [12] S. Leong, A. Razmjou, K. Wang, K. Hapgood, X. Zhang, H. Wang, J. Membr. Sci. 472 (2014) 167–184.
- [13] J.C. Yu, J. Yu, W. Ho, Z. Jiang, L. Zhang, Chem. Mater. 14 (2002) 3808–3816.
- [14] J. Wang, F. Cao, Z. Bian, M.K.H. Leung, H. Li, Nanoscale 6 (2014) 897–902.
- [15] C.C. Klick, Phys. Rev. 89 (1953) 274–277.
- [16] J. Yu, J. Xiong, B. Cheng, S. Liu, Appl. Catal. B 60 (2005) 211–221.
- [17] G. Liu, Y. Zhao, C. Sun, F. Li, G.Q. Lu, H.M. Cheng, Angew. Chem. Int. Ed. 47 (2008) 4516–4520.
- [18] K. Sridharan, E. Jang, T.J. Park, Appl. Catal. B 142–143 (2013) 718–728.
- [19] L. Gu, J. Wang, Z. Zou, X. Han, J. Hazard. Mater. 268 (2014) 216–223.
- [20] X. Wang, S. Blechert, M. Antonietti, ACS Catal. 2 (2012) 1596–1606.
- [21] H. Li, Y. Liu, X. Gao, C. Fu, X. Wang, ChemSusChem 8 (2015) 1189–1196.
- [22] K. Maeda, X. Wang, Y. Nishihara, D. Lu, M. Antonietti, K. Domen, J. Phys. Chem. C 113 (2009) 4940–4947.
- [23] H. Wang, X. Yuan, Y. Wu, G. Zeng, X. Chen, L. Leng, H. Li, Appl. Catal. B 174–175 (2015) 445–454.
- [24] Y. Wang, X. Wang, M. Antonietti, Angew. Chem. Int. Ed. 51 (2012) 68–89.
- [25] A. Thomas, A. Fischer, F. Goettmann, M. Antonietti, J.O. Müller, R. Schlögl, J.M. Carlsson, J. Mater. Chem. 18 (2008) 4893–4908.
- [26] Y. Zheng, J. Liu, J. Liang, M. Jaroniec, S.Z. Qiao, Energy. Environ. Sci. 5 (2012) 6717–6731.

- [27] F. Chang, J. Zhang, Y. Xie, J. Chen, C. Li, J. Wang, J. Luo, B. Deng, X. Hu, *Appl. Surf. Sci.* 311 (2014) 574–581.
- [28] C. Han, Y. Wang, Y. Lei, B. Wang, N. Wu, Q. Shi, Q. Li, *Nano. Res.* 8 (2015) 1199–1209.
- [29] J. Zhou, M. Zhang, Y. Zhu, *Phys. Chem. Chem. Phys.* 17 (2015) 3647–3652.
- [30] S. Zhou, Y. Liu, J. Li, Y. Wang, G. Jiang, Z. Zhao, D. Wang, A. Duan, J. Liu, Y. Wei, *Appl. Catal. B* 158–159 (2014) 20–29.
- [31] S.C. Yan, Z.S. Li, Z.G. Zou, *Langmuir* 25 (2009) 10397–10401.
- [32] X. Wang, K. Maeda, A. Thomas, K. Takanabe, G. Xin, J.M. Carlsson, K. Domen, M. Antonietti, *Nat. Mater.* 8 (2009) 76–80.
- [33] M. Groenewolt, M. Antonietti, *Adv. Mater.* 17 (2005) 1789–1792.
- [34] Y. Li, J. Wang, Y. Yang, Y. Zhang, D. He, Q. An, G. Cao, *J. Hazard. Mater.* 292 (2015) 79–89.
- [35] Y. Chen, W. Huang, D. He, Y. Situ, H. Huang, *ACS Appl. Mater. Interf.* 6 (2014) 14405–14414.
- [36] J.Y. Park, L.R. Baker, G.A. Somorjai, *Chem. Rev.* 115 (2015) 2781–2817.
- [37] X. Zhu, N.R. Monahan, Z. Gong, H. Zhu, K.W. Williams, C.A. Nelson, *J. Am. Chem. Soc.* 137 (2015) 8313–8320.
- [38] Y.C. Lin, T.E. Chien, K.L. Li, J.L. Lin, *J. Phys. Chem. C* 119 (2015) 8645–8651.